International Journal of
Nanoscience and Nanotechnology

Research Article 2025, Volume 21, Issue 3

Solvothermal Synthesis and Characterization of $CsPbI_3$, $CsSnI_3$, and $CsPb_{1-x}SnxI_3$ Perovskite Nanocrystals

Hari Ganesha Y [1], Ramaraja Varma V [2], Gopalakrishna Naik K[1*]

Received 11 August 2025
Accepted 25 September 2025

DOI: 10.22034/ijnn.2026.2068417.2695

International Journal of Nanoscience and Nanotechnology

Abstract

Cesium lead iodide ($CsPbI_3$), cesium tin iodide ($CsSnI_3$), and $CsPb_{1-x}Sn_xI_3$ metal-halide perovskite (MHP) nanoparticles were synthesized by a solvothermal method. The powder X-ray diffraction (XRD) patterns of the synthesized $CsPbI_3$ and $CsSnI_3$ were found to correspond to α-$CsPbI_3$ and black γ-$CsSnI_3$ perovskite phases, respectively. The nanoparticles synthesized from equimolar amounts of Pb and Sn precursors indicated the formation of α-$CsPbI_3$, black γ-$CsPbI_3$, and black γ-$CsSnI_3$ perovskite phases instead of the formation of the intended quaternary $CsPb_{0.5}Sn_{0.5}I_3$ solid solution. The field emission scanning electron microscopy (FESEM) images showed the formation of nanorods for $CsPbI_3$, nanorods and nanoplatelets for $CsSnI_3$, and nanorods/ nanowires and nanoplatelets for the intended $CsPb_{0.5}Sn_{0.5}I_3$ nanostructures. The Fourier transform infrared (FTIR) spectra of the synthesized samples showed the presence of the oleic acid ligand used in synthesis as a surfactant in the synthesized nanostructures. The estimated band gaps of the synthesized α-$CsPbI_3$ and B-γ-$CsSnI_3$ nanostructures from the UV-visible optical absorption measurements were found to be slightly higher than the reported bulk band gap values of these materials, which may be due to the quantum confinement effect. The exciton-related absorptions were observed both in α-$CsPbI_3$ and B-γ-$CsSnI_3$ nanostructures. The band gaps of both α-$CsPbI_3$ and B-γ-$CsSnI_3$ nanostructures were found to show a blue shift as the nanostructures undergo aging, which may be due to the predominance of the band-to-band absorption over the excitonic absorption with aging of the nanostructures. The synthesized nanostructures appear to exhibit long-term structural stability, as confirmed by the observation of stable XRD patterns and UV-visible optical absorption spectra of the synthesized samples for a period of four to six months after the synthesis.

Keywords: Perovskite, Solvothermal, $CsPbI_3$, $CsSnI_3$

How to cite this article

Hari Ganesha Y, Ramaraja Varma V, Gopalakrishna Naik K. Solvothermal Synthesis and Characterization of $CsPbI_3$, $CsSnI_3$, and $CsPb_{1-x}SnxI_3$ Perovskite Nanocrystals. Int. J. Nanosci. Nanotechnol., 2025;3: 137-148. DOI: 10.22034/ijnn.2026.2068417.2695

1. Introduction

Since the late 1990s, the MHPs have been attracted considerable attention for applications such as solar cells, light-emitting diodes, lasers, photodiodes, and photocatalysts due to their excellent optoelectronic properties [1]. The metal-halide perovskites (MHPs) are described by the general chemical formula ABX_3, where A and B are the cations and X is the halide anion. The MHPs, in general, are classified into two main classes: organic-inorganic hybrid MHPs and inorganic MHPs [1-2]. In organic-inorganic hybrid MHPs, A-site is occupied by an organic monovalent cation such as methylammonium ($CH_3NH_3^+$, MA^+) or formamidinium ($CH(NH_2)_2^+$, FA^+), and the A-site in inorganic MHPs consists of inorganic-metal cesium (Cs^+) or rubidium (Rb^+) cations [1-3]. In both the above classes, the B-site consists of divalent metal cations such as lead (Pb^{2+}), tin (Sn^{2+}), germanium (Ge^{2+}), strontium (Sr^{2+}), and calcium (Ca^{2+}). The X-site consists of a halide anions such as I^-, Br^-, or Cl^- in both the above classes of MHPs [1-3]. In 2009, Kojima et al., first used MHPs as visible-light sensitizers in solar cells [4]. Since then, progress in the study of lead-halide perovskites for solar cell applications has increased significantly. In 2012, Kim et al. reported, for the first time, all-solid-state perovskite solar cells using organic-inorganic MHPs [5]. Currently, the progress in MA- and FA-based lead halide perovskite organic-inorganic MHP nanocrystal (NC) solar cells has resulted in a photo conversion efficiency (PCE) of about 25 to 26% under laboratory conditions [1,6,7]. However, the instability of MA and FA based lead halide perovskite organic-inorganic hybrid MHPs under environmental conditions and toxicity had limited these materials for solar cell applications. Recently, all-inorganic semiconducting MHPs such as $CsPbX_3$ (X = Cl, Br, and I) NCs have emerged as ideal materials for optoelectronic applications including solar cells, light-emitting diodes,

[1] *A1 Department of Studies in Physics, Mangalore University, Mangalagangothri – 574 199, India*

[2] *Microtron Centre, Department of Studies in Physics, Mangalore University, Mangalagangothri – 574 199, India*

E-mail: gopal1mng@gmail.com

lasers, and photodetectors. Compared to the organic-inorganic hybrid MHPs, the inorganic metal halide perovskites show higher melting points, higher thermal stability, and enhanced photophysical properties [1,8]. Protesescu et al. for the first-time synthesized the $CsPbX_3$ NCs in 2015 using a hot-injection method [9]. Since then, $CsPbX_3$ NCs have been prepared using solution and vapor-phase growth methods by various researchers [1,10]. The solution-based methods include hot injection, ligand-assisted precipitation, solvothermal, microfluidics, and spin coating [1,11]. The parameters like precursors, surface ligands, synthesis duration, and synthesis temperature were optimized by various researchers during the solution-based synthesis to obtain the desired properties of the synthesized all-inorganic perovskite NCs [9,11]. Among the $CsPbX_3$ perovskites, the cubic $CsPbI_3$ (a-$CsPbI_3$) has an energy band gap of about 1.73 eV at room temperature [12]. The solar spectral matching of the energy band gap, the excellent optical properties, and ease of synthesis have attracted considerable attention for perovskite perovskite a-$CsPbI_3$ as a promising material for high-performance solar cells [13,14]. However, a-$CsPbI_3$ has the problem of room temperature instability [13,15] and the high toxicity of Pb [16]. $CsPbI_3$ is known to have four structural phases: the room temperature non-perovskite orthorhombic phase known as the d-phase or yellow phase (Y-$CsPbI_3$), and three high temperature perovskite phases with cubic (α-phase), tetragonal (β-phase), and orthorhombic (γ-phase) structures [13,15]. The non-perovskite orthorhombic d-phase and perovskite cubic phase (α-phase) are the most commonly observed crystal phases of $CsPbI_3$ [13]. The perovskite cubic phase of $CsPbI_3$ is known to be stable only above a temperature of 300 °C and as the temperature decreases it undergoes a structural phase transition via the high-temperature metastable perovskite tetragonal b-$CsPbI_3$, followed by orthorhombic black g-$CsPbI_3$ (B-g-$CsPbI_3$) phase, to the room-temperature stable non-perovskite d-$CsPbI_3$ phase [17]. The d-$CsPbI_3$ with an energy band gap of around 2.82 eV, along with poor optical properties, is not a suitable material for optoelectronic applications [13]. Researchers are exploring strategies such as thermal engineering [15], surface treatments/surface modifications [15,17–20], composition engineering [13,17,19], use of size-controlled nanostructures [9,18,21,22], and strain engineering [13,23] for room temperature stabilization of the perovskite phases of $CsPbI_3$. The report of Protesescu et al. [9] in 2015 is an example of the size-controlled synthesis of room temperature stable $CsPbX_3$ NCs. Similarly, Swarnkar et al. [21] in 2016 reported the quantum-dot-induced stability of a-$CsPbI_3$ perovskite. Zhang et al. reported highly luminescent and stable perovskite $CsPbI_3$ NCs with sodium dodecyl sulfate (SDS) ligand passivation using the hot-injection method [24]. Chen et al. reported highly luminescent and stable perovskite $CsPbI_3$ NCs using TOPO as a ligand [25]. Chen et al. reported the synthesis of highly luminescent cubic $CsPbI_3$ via a hot-injection method based on a hydrogen lead trihalide ($HPbI_3$) intermediate compound, using hydrogen iodide (HI), PbI_2, N,N-dimethylformamide, Cs_2CO_3, octadecene, oleic acid, and oleylamine as precursors [26]. Wen et al. reported the highly luminescent and stable a-$CsPbI_3$ nanorods synthesized by the solvothermal method [27].

To overcome the toxicity of lead, the development of lead-free all-inorganic cesium halide-based semiconductor perovskite materials by replacing Pb^{2+} ions with Sn^{2+} and Ge^{2+} ions in $CsPbX_3$ has received attention [1]. Among the all-inorganic lead-free cesium halides, cesium tin halide nanomaterials such as $CsSnI_3$ [28–30], $CsSnCl_3$ [31], $CsSnBr_3$ [32], and $CsSnBr_2Cl$ are widely investigated [33]. Also, the partial replacement of Pb^{2+} with Sn^{2+} in $CsPbX_3$ to produce perovskite nanostructures with optical properties similar to the cubic $CsPbX_3$ nanostructures has been an active area of research [17]. Similar to perovskite $CsPbX_3$, the $CsSnX_3$ perovskite phase is not stable at room temperature. For example, $CsSnI_3$ is known to have four structural phases: two orthorhombic phases, the one-dimensional non-perovskite Y-phase, and three-dimensional perovskite black g-phase, are co-existing at room temperature and two high temperature phases, the tetragonal black b-phase and the black a-phase [28–30]. Upon heating, the black g-$CsSnI_3$ is reported to undergo a structural phase transition at 362 K to black b-phase and then to a black a-phase at around 440 K [28–30]. The black g-phase is reported to transform into one-dimensional non-perovskite Y-phase when exposed to air at room temperature; the Y-phase $CsSnI_3$ is reported to transform to black a-phase when heated above 425 K, and upon subsequent cooling, the cubic phase transforms through black tetragonal b-phase to black g-phase [28–30]. The perovskite B-g-$CsSnI_3$ is known to be a direct band gap semiconductor material with a band gap energy of 1.3 eV at room temperature and has excellent optical properties for various optoelectronic applications [28–30,34,35]. However, perovskite B-g-$CsSnI_3$ also has the problem of rapid oxidation of Sn^{2+} to Sn^{4+} when exposed to air and resulting in the degradation of its optoelectronic properties [36]. To overcome the instability of the perovskite phase of $CsSnX_3$ and oxidation of Sn^{2+} to Sn^{4+}, researchers are also using strategies such as additive engineering, composition regulation, and use of proper synthesis methods [35,37]. Ali et al. discussed the lead-free $CsSnCl_3$ perovskite nanocrystals synthesis by adopting a rapid hot-injection technique and showed thermal stability of the as-synthesized $CsSnCl_3$ sample over a wide temperature range (30–280 °C) by conducting TGA and DSC measurements [31]. Adib et al. discussed the synthesis of stable cubic perovskite $CsSnBr_3$ nanocrystals by adopting a rapid hot-injection technique through bismuth doping and they showed thermal stability of the as-synthesized $CsSnBr_3$ sample up to around 400 °C by TGA measurement [32]. Yasmeen et al. discussed the moisture-stable $CsSnBr_3Cl$ nanocrystals synthesis by adopting a rapid hot-injection technique and demonstrated its stability even after 75 days of water immersion [33]. Cao et al. showed the stability enhancement of lead-free $CsSnI_3$ perovskite photodetector with reductive ascorbic acid additive [38]. Benaicha et al. discussed enhanced structural stability and optoelectronic properties of lead-free α-phase $CsSnI_3$ perovskite via Zn and Cu doping [39]. Dilshod et al. report preparation of air stable lead-free $CsSnI_3$ perovskites: synthesis based on CsI and $SnCl_2$ solutions [40].

The hot-injection and solvothermal techniques are the prominent methods for preparing $CsPbX_3$ and $CsSnX_3$ nanocrystals. The purpose of the present work was an attempt to synthesize long-term stable $CsPbI_3$ and $CsSnI_3$ nanoparticles for solar cell applications. In the present study, $CsPbI_3$ and $CsSnI_3$ nanoparticles were synthesized using solvothermal method, using a procedure somewhat similar to that described by Wen et al. [27] for the synthesis of $CsPbI_3$. The synthesized nanomaterials were characterized using powder XRD, FESEM, FTIR, and UV-visible absorption spectroscopy. Also, the synthesis of $CsPb_{1-x}Sn_xI_3$ was attempted using equal molar ratios of PbI_2 and SnI_2, respectively, as Pb and Sn sources. However, the XRD patterns of the synthesized nanoparticles demonstrate the formation of the cubic a-$CsPbI_3$, orthorhombic black-g-$CsPbI_3$, and the orthorhombic black -g-$CsSnI_3$ nanostructures instead of solid solution of $CsPb_{1-x}Sn_xI_3$. The solvothermal synthesis of $CsPbI_3$ and $CsSnI_3$ resulted in the formation of long-term stable α-$CsPbI_3$ and B-γ-$CsSnI_3$ phase nanostructures.

2. Experimental

2.1 Materials

Cesium carbonate (Cs_2CO_3, TCI), lead(II) iodide (PbI_2, TCI), tin(II) iodide (SnI_2) (TCI), 1-octadecene (1-ODE, Sigma Aldrich), oleic acid (OA, TCI), oleylamine (OLA, TCI) were used for the synthesis of cesium lead-tin iodide perovskite nanocrystals by the solvothermal method.

2.2 Preparation of precursor solutions

Precursor solutions were prepared using a method adapted from Wen et al. [27] for the synthesis of $CsPbI_3$ and $CsSnI_3$ nanoparticles as discussed below.

2.2.1 Cesium Oleate (CsOL) preparation

Wen et al. [27] prepared the cesium oleate precursor by following the procedure of Protesescu et al. [9], under ambient conditions instead of in an inert gas atmosphere. The procedure of Wen et al. was adopted in the present work to prepare the CsOL precursor [27]. In a 100 mL three-neck round bottom flask, 0.653 g (2 mmol) of cesium carbonate (Cs_2CO_3), 18 mL of 1-ODE, and 2.5 mL of OA were added to prepare CsOL. The resulting mixture was subjected to heating at 150 °C for 30 minutes in open air with continuous stirring at 500 rpm. Subsequently, the solution was allowed to cool to room temperature.

2.2.2 Preparation of PbI_2 precursor

For the preparation of PbI_2 precursor solution, 0.922 g (2 mmol) of PbI_2, 20 mL of 1-ODE, 3 mL of OA, and 3 mL of OLA were added to a 100 mL 3-neck round-bottom flask and stirred at 1000 rpm at 150 °C for 60 minutes under open air using a magnetic hotplate stirrer.

2.2.3 Preparation of SnI_2 precursor

The SnI_2 precursor solution was prepared using 0.745 g (2 mmol) of SnI_2, 20 mL of 1-ODE, 3 mL of OA, and 3 mL of OLA in a 100 mL 3-neck round-bottom flask. The precursor solution temperature was maintained at 150 °C under open-air conditions for 60 min under constant stirring at 1000 rpm using a magnetic hotplate stirrer.

2.2.4 Preparation of SnI_2-PbI_2 precursor

In a 100 mL 3-neck round-bottom flask 0.373 g (1 mmol) of SnI_2, 0.461 g (1 mmol) of PbI_2, 20 mL of 1-ODE, 3 mL of OA, and 3 mL of OLA were combined. OA and OLA were found to be essential for dissolving the precursors and also used for stabilizing the synthesized nanocrystals [9]. The resulting mixture was consistently stirred at 1000 rpm at 150 °C for 60 minutes under open air using a magnetic hotplate stirrer.

2.3 Solvothermal synthesis of $CsPbI_3$, $CsSnI_3$, $CsPb_{1-x}Sn_xI_3$ nanocrystals

For the synthesis of $CsPbI_3$, $CsSnI_3$, and $CsPb_{1-x}Sn_xI_3$ nanocrystals, for each of the prepared PbI_2, SnI_2, and PbI_2–SnI_2 precursor solutions, 2 mL of the prepared CsOL solution was added under continuous stirring at room temperature for 5 min and loaded into a Teflon-lined autoclave (100 mL). The solvothermal growth of $CsPbI_3$, $CsSnI_3$, and $CsPb_{1-x}Sn_xI_3$ nanostructures using the respective precursor solutions was carried out at 150 °C for 60 minutes. After the solvothermal growth, the solution was centrifuged and washed with n-hexane 3 to 5 times to remove the unreacted precursors. Each of the resulting nanostructures was dried at 150 °C for 14 hours in ambient conditions.

2.4 Characterization

The powder XRD pattern was recorded using a Rigaku Miniflex 600 benchtop X-ray diffractometer with a CuK_a (l = 0.15406 nm) X-ray source. FTIR measurements were performed on a Shimadzu IRSpirit Fourier transform infrared spectrophotometer. The FESEM studies were acquired using a Zeiss Gemini Sigma 300 system. Energy-dispersive X-ray spectroscopy (EDX) was performed using the EDX detector attached to the Sigma 300 FESEM. The UV-visible optical absorption measurements were carried out using a Shimadzu UV-1800 spectrophotometer. Due to the temporary unavailability of the characterization facilities, the synthesized nanocrystals could not be characterized right after the synthesis; all characterizations were carried out several days after the synthesis.

3. Results and Discussion

3.2 X-ray diffraction spectroscopy

Fig. 1(a) and 1(b) show the powder XRD patterns of the synthesized $CsPbI_3$ nanostructures, which were stored in ambient air for 50 and 150 days after synthesis, respectively. The appearance of the well-resolved XRD pattern even after a prolonged period following synthesis indicates the long-term stability of the synthesized nanostructures in ambient air. Compared with previously reported data, the XRD peaks appearing at 2θ values of 14.01°, 20.05°, 25.81°, 28.41°, 32.51°, 36.01°, 40.91°, and 42.51° in Fig. 1 could be assigned to the (100), (110), (111), (200), (210), (211), (220), and (300) planes of α-$CsPbI_3$, respectively [41–43]. The observation of the well-resolved XRD patterns even after 150 days after the synthesis indicates the long-term stability of the

synthesized a-$CsPbI_3$ nanostructures.

The low-intensity XRD peaks observed at 2θ values of 23.86°, 27.25°, and 48.57° in Fig. 1 can be assigned to the (100), (110), and (211) planes of CsI, respectively [44]. The XRD peaks observed at 2θ values of 38.58° and 53.04° can be assigned to (003) and (004) planes of PbI_2[45]. The presence of CsI and PbI_2 may be due to the incomplete conversion of the CsI and PbI_2 precursors into $CsPbI_3$ or due to the slow decomposition of $CsPbI_3$ into CsI and PbI_2 upon aging. There are reports in the literature on the long-term stability of a-$CsPbI_3$ nanocrystals under ambient air [9,18,20,46]. Swarnkar et al. reported the synthesis of α-$CsPbI_3$ quantum dots (QD) thin films having long-term ambient air stability and demonstrated stable XRD and optical absorption for these films stored in ambient air for a period of 60 days [21]. Li et al. reported the synthesis of long-term stable a-$CsPbI_3$ nanostructured films by poly-vinylpyrrolidone (PVP) surface passivation and presented the stable XRD pattern of such a-$CsPbI_3$ nanostructured film after 80 days [18]. Dutta et al. reported ambient air stable synthesis of a-$CsPbI_3$ nanostructure by hot-injection method at a temperature higher than the typical hot-injection synthesis temperature using OLA and hydroiodic acid, and replacing the ice-cooling process with extended thermal annealing at the synthesis temperature [47]. The oleylamine (OLA) surfactant binding on the nanocrystals is reported to be dynamic, may desorb during isolation by centrifugation and purification process [48]. In nanoscale metal halide perovskites, it has been believed that the high surface-to-volume ratio related surface stress can lead to sufficient tensile strain so that the crystal remains in the perovskite structural phase at room temperature [21,22]. Therefore, the observed long-term phase stability of the synthesized a-$CsPbI_3$ in the present work may be due to their nano-dimensions [9,20,22].

Fig. 2(a) and 2(b) show the XRD patterns of the synthesized $CsSnI_3$ nanostructures, which were stored in ambient air for 48 days and 151 days after the synthesis, respectively. In comparison with literature, the peaks observed at 2θ values of 14.91°, 20.97°, 23.01°, 24.01°, 25.51°, 27.51°, 29.01°, 32.41°, 36.49°, 38.37°, 42.15°, 45.15°, 51.57°, and 54.65° could be assigned to (101), (200), (201), (211), (220), (221), (202), (103), (321), (033), (242), (421), (440), and (423) planes of the perovskite black orthorhombic phase $CsSnI_3$ (B-g-$CsSnI_3$) nanostructures, respectively [49–52]. The additional peaks observed at 2θ values of 39.32°, 48.68°, and 56.92° could be assigned to (200), (211), and (220) planes of CsI, respectively [44,53]. The CsI may be present either because the CsI precursor was not fully converted into $CsSnI_3$ or because $CsSnI_3$ slowly decomposed into CsI for a long time after synthesis. The XRD patterns of the hydrothermally synthesized B-g-$CsSnI_3$ nanostructures shown in Fig. 2 also indicate the long-term stability of the nanostructures under ambient conditions.

Fig. 3 presents the XRD patterns of the perovskite nanostructures synthesized using CsOL along with equimolar amounts of PbI_2 and SnI_2 precursors, recorded at (a) 28 days and (b) 122 days post-synthesis, respectively. Comparing the XRD pattern shown in Fig. 3 with the literature indicates the growth of α-$CsPbI_3$ [41,42], B-γ-$CsPbI_3$ [54], and B-γ-$CsSnI_3$ [49–52] nanoparticles structures instead of the intended quaternary $CsPb_{0.5}Sn_{0.5}I_3$ nanoparticles. The XRD peaks observed at 2θ values of 14.01°, 20.05°, 25.51°, 28.41°, 32.47°, 36.01° and 40.91° are assigned to the (100), (110), (022), (200), (210), (211) and (220) planes of α-$CsPbI_3$ (represented as aPb in Fig. 3), respectively [41–43]. The XRD peaks observed at 2θ values of 23.01°, 24.01°, and 29.01° are assigned to the (120), (121), and (220) planes of B-γ-$CsPbI_3$ (represented as gPb in Fig. 3), respectively [54]. The XRD peaks observed at 2θ values

of 14.91°, 23.01°, 24.01°, 25.51°, 27.19°, 29.01°, 32.47°, 42.15°, 45.09°, 51.49° and 54.67° are assigned

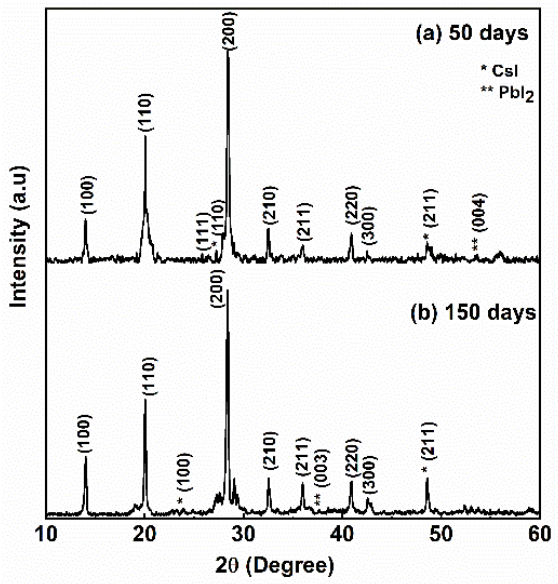

Figure 1. XRD patterns of the synthesized α-CsPbI3 nanostructures recorded (a) 50 days, and (b) 150 days after synthesis.

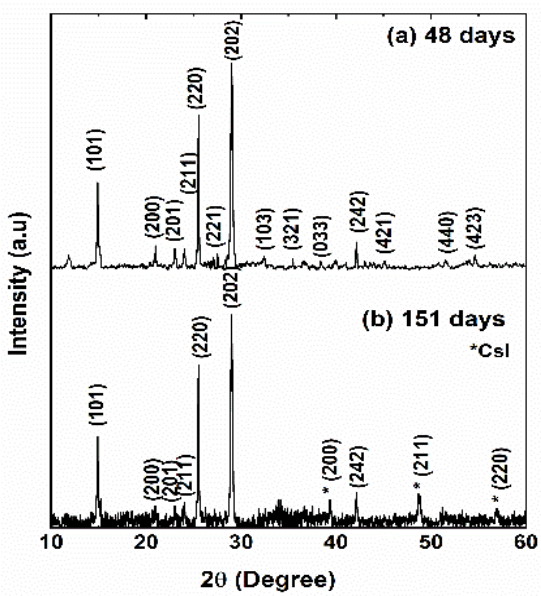

Figure 2. The XRD pattern of the synthesized B-(-CsSnI3 nanostructures recorded (a) 48 days, and (b) 151 days after synthesis.

to (101), (201), (211), (220), (122), (103), (242), (421), (440) and (423) planes of B-γ-$CsSnI_3$ (represented as γSn in Fig. 3), respectively [49–52]. Dimesso et al. report the observation of orthorhombic B-g-$CsSnI_3$ phase for the $CsSn_{1-x}Pb_xI_3$ powder annealed in nitrogen at 270 °C for 8 hours, they also observed this phase in samples with a Pb composition range 0.0 £ x £ 0.1, and noted that the XRD pattern of samples with $x \geq 0.3$ resembled the orthorhombic phase very similar to that of the $CsPbI_3$ perovskite, synthesized by self-organization process in aqueous solutions [55]. Zhang et al. reported the synthesis of strongly confined $CsSn_xPb_{1-x}I_3$ ($CsSn_{0.09}Pb_{0.91}I_3$) quantum dots by room temperature colloidal synthesis [56]. The presence of CsI and PbI_2 XRD peaks in the synthesized nanoparticles could be from either the incomplete conversion of the $CsSnI_3$ or $CsPbI_3$ precursors into $CsSnI_3$ and $CsPbI_3$ perovskite nanoparticles, respectively, or from the decomposition of the $CsPbI_3$ and $CsSnI_3$ perovskite nanoparticles occurring gradually after the synthesis. The XRD pattern shown in Fig. 3 also indicates the long-term stability of the synthesized a-$CsPbI_3$, g-$CsPbI_3$, and g-$CsSnI_3$ nanostructures. The crystallite size of the synthesized nanostructures was calculated from the XRD pattern using Scherrer's equation [57]. Scherrer's equation is given by

$$D = \frac{k}{cos} \quad (1)$$

where l is the wavelength of the X-Ray radiation used for recording the XRD pattern (CuKa =0.15406 nm), β is FWHM (full width at half maximum) of the XRD peak in radians, θ is the Bragg angle of diffraction, D is crystallite size (nm), and k is a constant crystallite shape factor (which equals to 0.9). The crystallite size of the a-$CsPbI_3$ and B-g-$CsSnI_3$ nanocrystals was calculated using the highest intensity (200) and (202) XRD peaks, respectively. The calculated crystallite sizes for the a-$CsPbI_3$ and B-g-$CsSnI_3$ nanocrystals were found to be around 31 nm and 28 nm, respectively. The d-spacing was calculated from the XRD data using Bragg's law. The microstrain e was calculated using the relation [57].

$$= \frac{hkl}{4tan} \quad (2)$$

The lattice parameters for the cubic a-$CsPbI_3$ were calculated using the relation

$$d_{hkl} = \frac{a}{\sqrt{h^2 + k^2 + l^2}} \quad (3)$$

We could not calculate the lattice parameters for the orthorhombic B-g-$CsSnI_3$ due to the unavailability of the required crystallographic information file (CIF) of B-g-$CsSnI_3$. The d-spacing, full width at half maximum (FWHM), crystallite size D, and strain e calculated using the XRD pattern are shown in Table 1 and Table 2 for a-$CsPbI_3$ and B-g-$CsSnI_3$ nanostructures, respectively. The calculated crystallite sizes for the a-$CsPbI_3$ using the highest intensity (200) XRD peak was found to be 31 nm. Over the aging time slight increase in FWHM, slight decrease in crystallite size, and a slight increase in microstrain e were observed. The calculated crystallite sizes for B-g-$CsSnI_3$ nanostructures using the highest intensity (202) XRD peaks was found to be 28 nm. However, no noticeable changes in FWHM, D, and e values in the calculated data could be observed over the aging time in B-g-$CsSnI_3$ nanostructures. The lattice parameter *a* for cubic a-$CsPbI_3$ calculated using Bragg's law with a d-spacing of 0.3138 nm for the (200) plane, is 0.6276 nm which agrees with the 0.624 to 0.626 nm range reported in the literature [58].

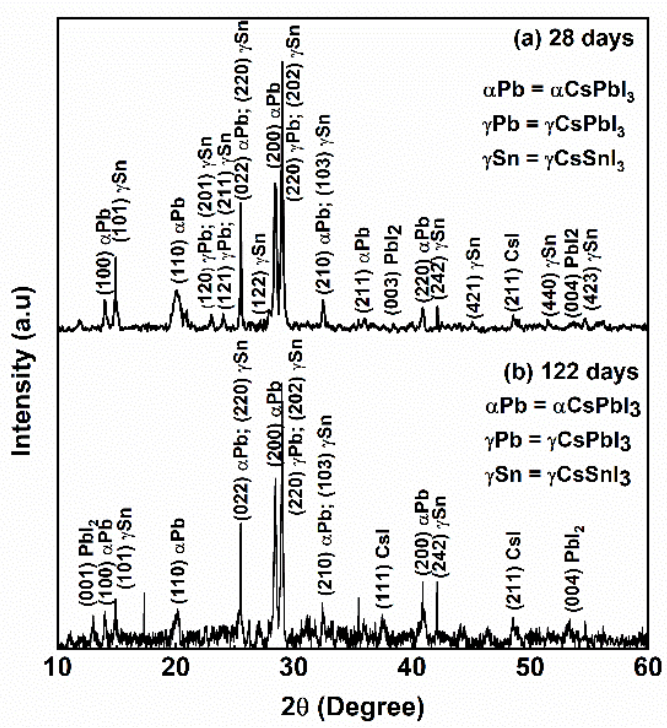

Figure 3. The XRD pattern of the CsPb1-xSnxI3 nanoparticles synthesized using equimolar ratios of PbI2 and SnI2 recorded: (a) 28 days, and (b) 122 days after synthesis.

3.3 Fourier-Transform Infrared spectroscopy

Fig. 4 Shows the FTIR spectra of synthesized (a) $CsPbI_3$, (b) $CsSnI_3$, and (c) $CsPbSnI_3$ nanostructures. The presence of the oleic acid and oleylamine surfactant on the synthesized perovskite $CsPbI_3$, $CsSnI_3$, and $CsPbSnI_3$ nanomaterials is confirmed by FTIR spectroscopy. In the FTIR spectra, IR absorption bands appeared around 2918 cm^{-1} and 2851 cm^{-1}, corresponding to the characteristic oleyl group of symmetric -CH_2 stretching and asymmetric -CH_2 stretching vibrations, respectively [59–63]. Therefore, the oleic acid and oleylamine ligands encapsulating the nanoparticles remain intact. The scissoring mode of the CH_2 group gives rise to a characteristic band near 1465 cm^{-1} in IR [61,62]. The peak at around 1568 cm^{-1} may be due to the C=O bond stretching [63].

3.4 Field effect scanning electron microscopy (FESEM)

Fig. 5(a) shows the FESEM images of the a-$CsPbI_3$ nano-rod-like structures with lengths on the order of several micrometres. Fig. 5(b) shows the EDX spectrum of the synthesized a-$CsPbI_3$ nanostructures, which displays the presence of Cs, Pb, and I elements and the compositions of elements in the synthesized nanostructures. Fig. 6(a) presents FESEM images of the B-g-$CsSnI_3$ nanostructures presenting the growth of nanorods and 2D nanoplates. The EDX spectrum in Fig. 6(b) confirms the presence of Cs, Sn, and I elements within the synthesized γ-$CsSnI_3$. The FESEM images of the intended $CsPb_{0.5}Sn_{0.5}I_3$ nanostructures shown in Fig. 7(a) indicate the growth of nanowires/nanorods and irregularly shaped 2D nanoplatelets. Fig. 7(b) shows the EDX spectrum of the

Table 1. CsPbI3 nanostructure parameters from XRD pattern.

50 days from the synthesis					
(hkl)	2θ	d (nm)	FWHM (2θ)	D (nm)	ε (×10^{-3})
(200)	28.41	0.3138	0.25	31.1	4.26
150 days from the synthesis					
(200)	28.39	0.3142	0.28	28.8	4.91

Table 2. CsSnI3 nanostructure parameters from XRD pattern.

48 days from the synthesis					
(hkl)	2θ	d (nm)	FWHM (2θ)	D (nm)	ε (×10^{-3})
(202)	29.01	0.3074	0.29	28.1	4.92
151 days from the synthesis					
(202)	29.01	0.3075	0.29	28.1	4.92

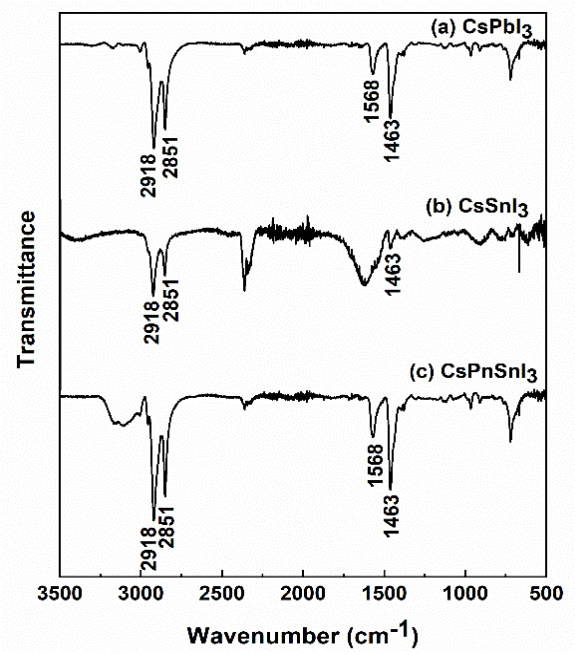

Figure 4. FTIR spectra of synthesized: (a) CsPbI3, (b) CsSnI3, and (c) CsPbSnI3 nanostructures.

synthesized $CsPb_{0.5}Sn_{0.5}I_3$, confirming the presence of Cs, Pb, Sn, and I and the compositions of elements in the synthesized nanostructures. The elemental compositions obtained from the EDX spectra further confirms the successful synthesis of $CsPbI_3$ and $CsSnI_3$ nanostructures.

3.5 UV-visible absorption spectroscopy

The synthesized nanostructures were dispersed in ethanol and placed in a cuvette for UV-visible optical absorption measurements. Fig. 8(a) – 8(c) show the UV-visible absorption spectra of the $CsPbI_3$ nanostructures recorded 7 days, 100 days, and 149 days after the synthesis, respectively. The appearance of an absorption peak at around 666 nm in the optical absorption spectrum of the $CsPbI_3$ nanostructures recorded 7 days after the synthesis, shown in Fig. 8(a), may be

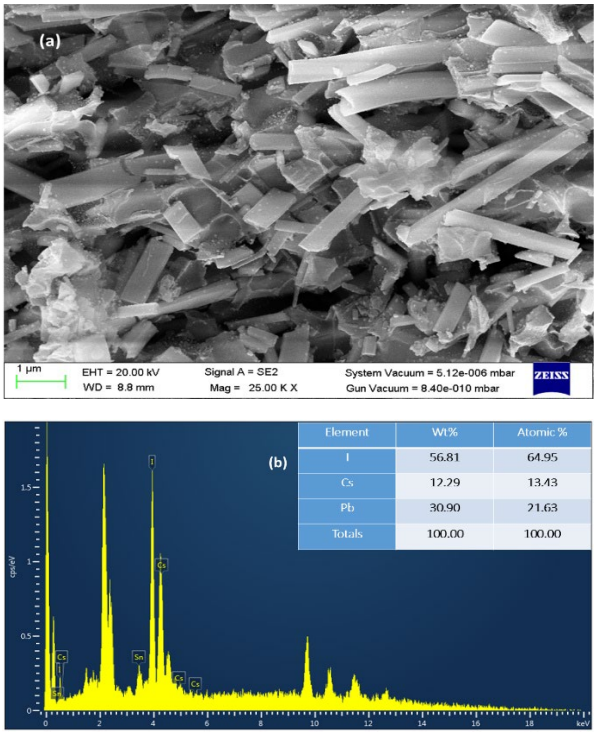

Figure 5. (a) FESEM image and (b) EDX spectrum of (-CsPbI3 nanostructures

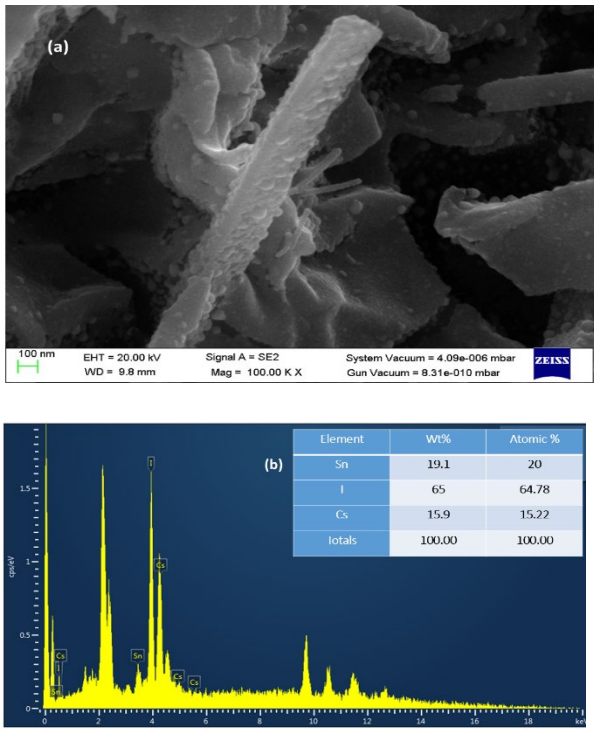

Figure 6. (a) FESEM image and (b) EDX spectrum of γ-$CsSnI_3$ nanostructures.

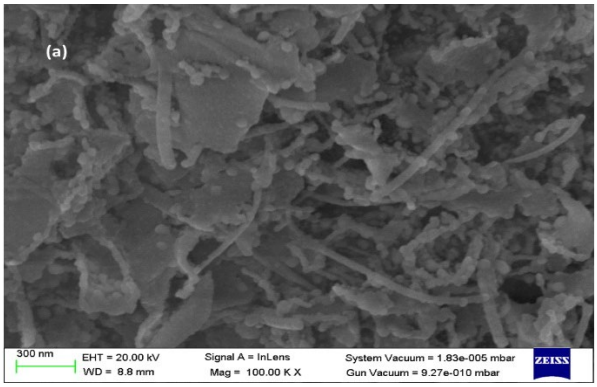

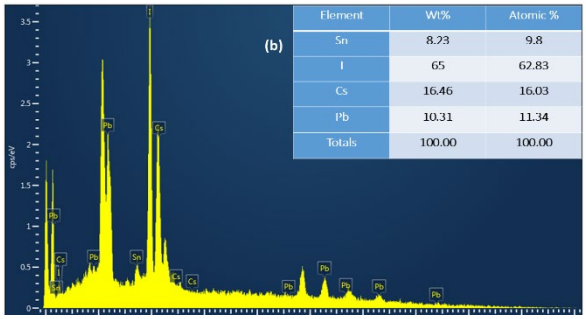

Figure 7. (a) FESEM image and (b) EDX spectrum of $CsPb_{1-x}Snxl_3$ nanostructures.

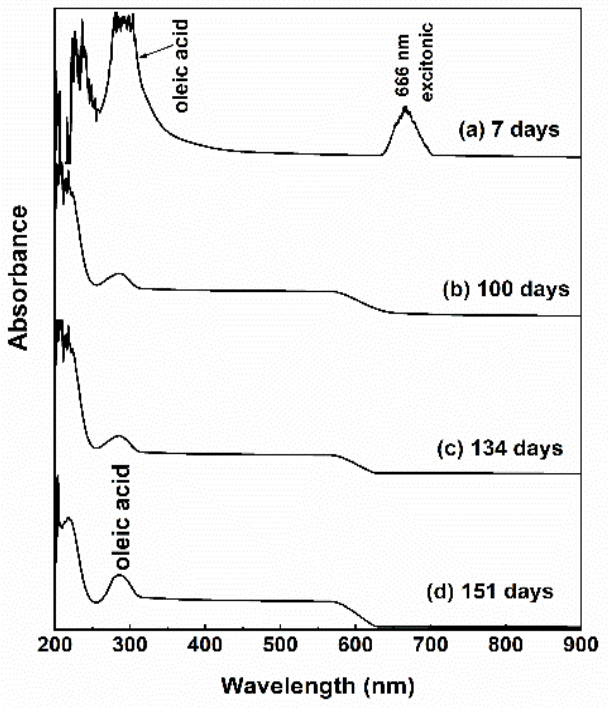

Figure 8. UV-visible absorption spectra of $CsPbI_3$ nanomaterials recorded (a) 7, (b) 100, (c) 134, and (d) 151 days after synthesis.

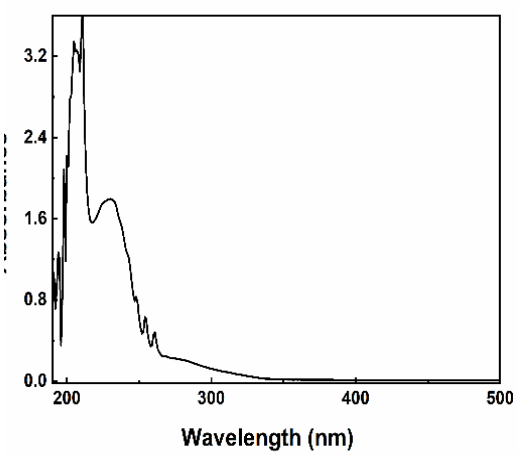

Figure 9. UV-visible optical absorption spectrum of oleic acid.

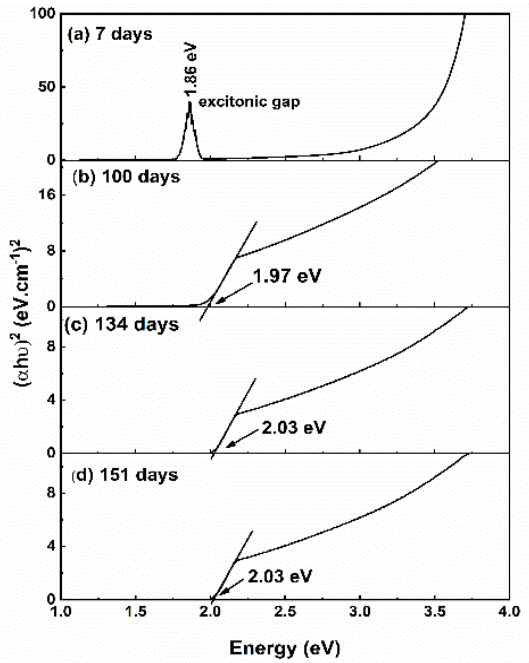

Figure 10. Tauc plots of UV-visible absorption data of CsPbI3 nanoparticles recorded (a) 7, (b) 100, (c) 134, and (d) 151 days after synthesis.

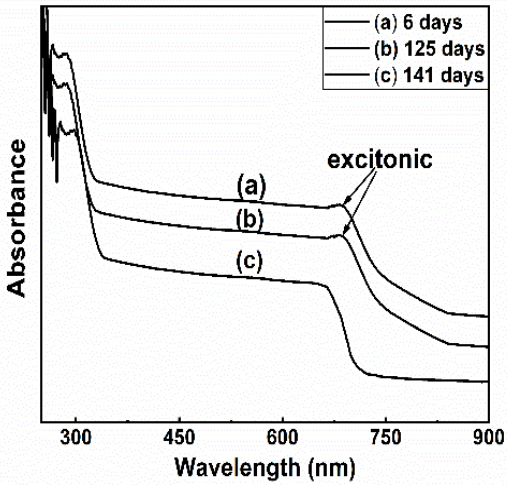

Figure 11. UV-visible absorption spectra of CsSnI3 nanomaterials recorded (a) 6, (b) 125, and (c) 141 days after synthesis.

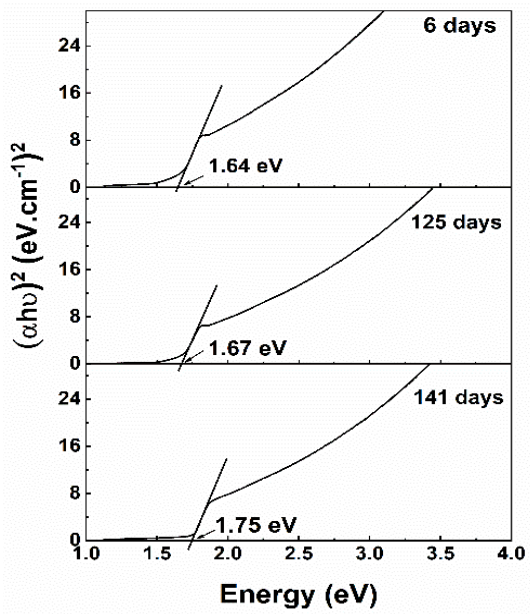

Figure 12. Tauc's plots of UV-visible absorption data of CsSnI3 nanoparticles recorded (a) 6, (b) 125, and (c) 141 days after synthesis.

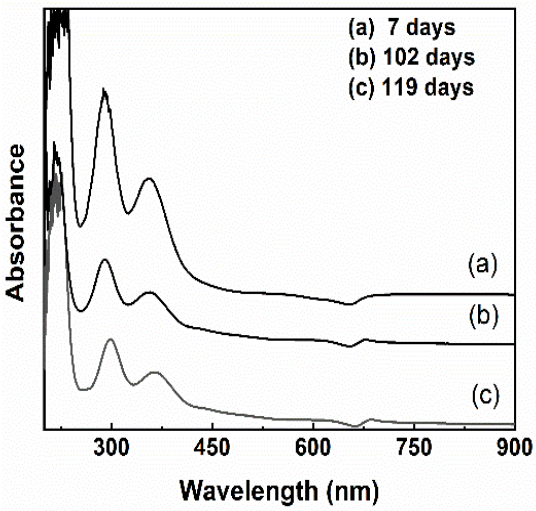

Figure 13. UV-visible absorption spectra of CsPbI3/CsSnI3 nanomaterials recorded (a) 7, (b) 102, and (c) 119 days after synthesis.

due to the formation of excitons in the synthesized a-$CsPbI_3$ nanostructures [21,29,41]. Exciton formation in semiconductor nanostructures often results in a significant increase in optical absorption just below the band gap energy [64]. There are many reports on the observation of excitonic-related absorbance peak in the cesium lead/tin halide perovskite nanostructures [1], such as reports of Protesescu et al. in the absorption spectra of 5 - 12 nm $CsPbBr_3$ nanocrystals [9], Swarnkar et al. in $CsPbI_3$ QDs [21], and Chung et al. in B-g-$CsSnI_3$ nanocrystals [28]. Similar observations have been reported in various $CsPbX_3$ systems, including cubic $CsPbI_3$ nanorods by Wen et al. [27], thin film $CsPbI_3$ deposited on FTO glass by Waleed et al. [41], and $CsPbBr_3$ nanocrystals Zhai et al. [65]. The optical absorption observed in the wavelength range £ 300 nm could be due to the oleic acid surfactant coating on the

nanomaterials [60]. To confirm the origin of this feature, the UV-visible spectrum of pure oleic acid (0.1 mL in 3.5 mL ethanol) was recorded (Fig. 9), which shows the strong oleic acid-related optical absorption below 300 nm wavelength. The band gap energy of the synthesized inorganic metal iodide perovskites was obtained from Tauc plots of UV-visible absorption data using the Tauc's equation $(h\nu)^{1/n} = A(h\nu - E_g)$ where A is a constant, a is optical absorption coefficient, *h* is the Planck's constant, n is the frequency of the light source used in the optical absorption measurement, and the constant factor n = 2 for the allowed optical transition in direct band gap semiconductors [66]. Fig. 10(a) to 10(c) show the Tauc's plots of the above UV-visible optical absorption spectra. The excitonic absorption band gap energy of $CsPbI_3$ can be calculated directly from the excitonic absorption peak wavelength 666 nm shown in Fig. 8(a) or obtained directly from the excitonic peak energy from the corresponding Tauc's plot shown in Fig. 10(a) and was found to be 1.86 eV for the synthesised a-$CsPbI_3$. The obtained excitonic absorption energy is much larger than the bulk band gap energy (1.73 eV), indicating the manifestation of strong quantum confinement in the synthesized a-$CsPbI_3$ nanostructures. Fig. 10(b) and 10(c) show the Tauc's plots of the UV-visible absorption data recorded 100 and 151 days after synthesis, and the energy band gaps were found to be 1.98 eV and 2.03 eV, respectively. The observed blue shift in the energy band gap with aging of the synthesized samples reflects a gradual decrease in the excitonic optical absorption. However, the quantum confinement-induced enhancement of the band gap over the bulk value appears to remain unchanged. As of now, we are unable to explain the reason for the suppression of excitonic optical absorption with aging of the sample, even though the size-dependent quantum confinement effect is clearly present in the synthesized α-$CsPbI_3$ nanostructures. Fig. 11(a) and 11(b) show the UV-visible absorption spectra of the synthesized $CsSnI_3$ of nanostructures recorded after 6 and 141 days from the synthesis, respectively. The small peak at the absorption edge of the spectrum shown in Fig. 11(a) also indicates the exciton formation in the synthesized B-g-$CsSnI_3$ nanostructure. Chung et al. also reported similar exciton-related absorption in $CsSnI_3$ nanocrystals [28]. Fig. 12(a) and 12(b) show the Tauc's plots of the corresponding absorption spectra, respectively. The corresponding energy band gaps estimated from the Tauc's plots are found to be 1.64 eV and 1.75 eV, respectively. The observed blue shift in band gap with an increase in storage time may be explained by the same argument as discussed above for the a-$CsPbI_3$ nanomaterials. As shown in Fig. 13(a) and 13(b), the UV-visible absorption spectra of the synthesized $CsPbSnI_3$ nanostructures recorded after 7 days and 119 days of the synthesis, respectively, are dominated by optical absorption peaks attributed to oleic acid. No characteristic absorptions feature corresponding to a-$CsPbI_3$, g-$CsPbI_3$, or g-$CsSnI_3$ were observed for the samples synthesized for $CsPb_{0.5}Sn_{0.5}I_3$.

4. Conclusion

The synthesis of $CsPbI_3$, $CsSnI_3$, and $CsPb_{0.5}Sn_{0.5}I_3$ nanostructures was carried out using the hydrothermal method. The hydrothermal synthesis of $CsPbI_3$ and $CsSnI_3$ resulted in the formation of long-term stable α-$CsPbI_3$ and B-γ-$CsSnI_3$ phase nanostructures, respectively, as confirmed by powder XRD measurements. The synthesized α-$CsPbI_3$ and B-γ-$CsSnI_3$ phase nanostructures were found to have much longer ambient stability compared to the previous reports in the literature. The long-term stability of the hydrothermally synthesized nanostructures may be due to the nanoscale morphologies. Since we have carried out the synthesis at only one growth temperature as discussed in the manuscript, it may be difficult to analyse the synthesis conditions which led to the long-term stability of the synthesized nanomaterials in this work. The intended synthesis of $CsPb_{0.5}Sn_{0.5}I_3$ nanostructures led to the formation of stable α-$CsPbI_3$, B-γ-$CsPbI_3$, and B-γ-$CsSnI_3$ phases. FESEM images of $CsPbI_3$ revealed the growth of nanorod-like structures with lengths of a few micrometers. In the case of $CsSnI_3$ nanostructures, FESEM images showed the formation of both nanorods and nanoplatelets. Similarly, FESEM images of the intended $CsPb_{0.5}Sn_{0.5}I_3$ nanostructures exhibited a mixture of nanorods/nanowires and nanoplatelets. The UV-visible absorption spectrum of α-$CsPbI_3$, measured seven days after synthesis, displayed a pronounced exciton-related absorption peak. A similar excitonic feature was also observed in the UV-visible absorption spectrum of the B-γ-$CsSnI_3$ nanostructures. The optical band gaps of the synthesized α-$CsPbI_3$ and B-γ-$CsSnI_3$, determined using Tauc plots, indicate the presence of quantum size effects in both nanostructures. Characteristic UV-visible absorption features related to oleic acid were observed in all synthesized nanostructures.

Acknowledgement

The Authors are grateful to the KSTePS-VGST program for providing access to the FTIR facility in the Department of Studies in Physics, the Microtron Centre for fluorescence spectroscopy, and the DST-PURSE lab for UV-Visible characterization at Mangalore University.

Funding sources

This research did not receive any specific grant from funding agencies in the public, commercial, or not-for-profit sectors.

Author contributions

Hari Ganesha Y: Writing - original draft (lead), **Gopalakrishna Naik K**: Writing - review and editing (supporting). **Ramaraja Varma V**: Formal analysis (supporting).

Conflict of interest

The authors declare that they have no known competing financial interests or personal relationships that could have appeared to influence the work reported in this paper.

Data availability

The datasets generated or analysed during this study are available from the corresponding author on reasonable request.

References

1. Dey A, Ye J, De A, Debroye E, Ha SK, Bladt E, et al. State of the Art and Prospects for Halide Perovskite Nanocrystals. ACS Nano. 2021;15(7):10775-10981. https://doi.org/10.1021/acsnano.0c08903
2. Hoefler SF, Trimmel G, Rath T. Progress on lead-free metal halide perovskites for photovoltaic applications: a review. Monatsh Chem. 2017;148(5):795-826. https://doi.org/10.1007/s00706-017-1933-9
3. Chen LJ. Synthesis and optical properties of lead-free cesium germanium halide perovskite quantum rods. RSC Adv. 2018;8(33):18396-18399. https://doi.org/10.1039/C8RA01150H
4. Kojima A, Teshima K, Shirai Y, Miyasaka T. Organometal Halide Perovskites as Visible-Light Sensitizers for Photovoltaic Cells. J Am Chem Soc. 2009;131(17):6050-6051. https://doi.org/10.1021/ja809598r
5. Kim HS, Lee CR, Im JH, Lee KB, Moehl T, Marchioro A, et al. Lead iodide perovskite sensitized all-solid-state submicron thin film mesoscopic solar cell with efficiency exceeding 9%. Sci Rep. 2012;2:591. https://doi.org/10.1038/srep00591
6. Wang R, Huang T, Xue J, Tong J, Zhu K, Yang Y. Prospects for metal halide perovskite-based tandem solar cells. Nat Photonics. 2021;15(6):411-425. https://doi.org/10.1038/s41566-021-00809-8
7. Tipparak P, Passatorntaschakorn W, Khampa W, Musikpan W, Usulor CE, Bhoomanee C, et al. The Impact of MAPbI3 Quantum Dots on CsFA Perovskite Solar Cells: Interface and Hole Extraction Improvement. ACS Appl Energy Mater. 2025;8(1):355-365. https://doi.org/10.1021/acsaem.4c02474
8. Zhang Q, Yin Y. All-Inorganic Metal Halide Perovskite Nanocrystals: Opportunities and Challenges. ACS Cent Sci. 2018;4(6):668-679. https://doi.org/10.1021/acscentsci.8b00201
9. Protesescu L, Yakunin S, Bodnarchuk MI, Krieg F, Caputo R, Hendon CH, et al. Nanocrystals of Cesium Lead Halide Perovskites (CsPbX3, X = Cl, Br, and I): Novel Optoelectronic Materials Showing Bright Emission with Wide Color Gamut. Nano Lett. 2015;15(6):3692-3696. https://doi.org/10.1021/nl5048779
10. Chen M, Zou Y, Wu L, Pan Q, Yang D, Hu H, et al. Solvothermal Synthesis of High-Quality All-Inorganic Cesium Lead Halide Perovskite Nanocrystals: From Nanocube to Ultrathin Nanowire. Adv Funct Mater. 2017;27(23):1701121. https://doi.org/10.1002/adfm.201701121
11. Xiang W, Tress W. Review on Recent Progress of All-Inorganic Metal Halide Perovskites and Solar Cells. Adv Mater. 2019;31(44):1902851. https://doi.org/10.1002/adma.201902851
12. Chen Z, Dong L, Tang H, Yu Y, Ye L, Zang J. Direct synthesis of cubic phase CsPbI3 nanowires. CrystEngComm. 2019;21(9):1389-1396. https://doi.org/10.1039/C8CE02111B
13. Wang B, Novendra N, Navrotsky A. Energetics, Structures, and Phase Transitions of Cubic and Orthorhombic Cesium Lead Iodide (CsPbI3) Polymorphs. J Am Chem Soc. 2019;141(37):14501-14504. https://doi.org/10.1021/jacs.9b05924
14. Idrissi S, Labrim H, Bahmad L, Benyoussef A. DFT and TDDFT studies of the new inorganic perovskite CsPbI3 for solar cell applications. Chem Phys Lett. 2021;766:138347. https://doi.org/10.1016/j.cplett.2021.138347
15. Ke F, Wang C, Jia C, Wolf NR, Yan J, Niu S, et al. Preserving a robust CsPbI3 perovskite phase via pressure-directed octahedral tilt. Nat Commun. 2021;12:461. https://doi.org/10.1038/s41467-020-20745-5
16. Ke W, Kanatzidis MG. Prospects for low-toxicity lead-free perovskite solar cells. Nat Commun. 2019;10:965. https://doi.org/10.1038/s41467-019-08918-3
17. Ustinova MI, Mikheeva MM, Shilov GV, Dremova NN, Frolova L, Stevenson KJ, et al. Partial Substitution of Pb2+ in CsPbI3 as an Efficient Strategy to Design Fairly Stable All-Inorganic Perovskite Formulations. ACS Appl Mater Interfaces. 2021;13(4):5184-5194. https://doi.org/10.1021/acsami.0c18061
18. Li B, Zhang Y, Fu L, Yu T, Zhou S, Zhang L, et al. Surface passivation engineering strategy to fully-inorganic cubic CsPbI3 perovskites for high-performance solar cells. Nat Commun. 2018;9:1076. https://doi.org/10.1038/s41467-018-03169-0
19. Min X, Xie Q, Wang X, Chen M. Enhancing the stability of cesium lead iodide perovskite nanocrystals: Recent progress, challenges and opportunities. Surfaces Interfaces. 2021;22:100870. https://doi.org/10.1016/j.surfin.2020.100870
20. Li D, Chen CS, Wu YH, Zhu ZG, Shih WY, Shih WH. Improving Stability of Cesium Lead Iodide Perovskite Nanocrystals by Solution Surface Treatments. ACS Omega. 2020;5(29):18013-18020. https://doi.org/10.1021/acsomega.0c01403
21. Swarnkar A, Marshall AR, Sanehira EM, Chernomordik BD, Moore DT, Christians JA, et al. Quantum dot-induced phase stabilization of α-CsPbI3 perovskite for high-efficiency photovoltaics. Science. 2016;354(6308):92-95. https://doi.org/10.1126/science.aag2700
22. Zhao Q, Hazarika A, Schelhas LT, Liu J, Gaulding EA, Li G, et al. Size-Dependent Lattice Structure and Confinement Properties in CsPbI3 Perovskite Nanocrystals: Negative Surface Energy for Stabilization. ACS Energy Lett. 2020;5(1):238-247. https://doi.org/10.1021/acsenergylett.9b02395
23. Le HKD, Lin CK, Jin J, Zhang Y, Lin Z, Vailionis A, et al. Quantification of strain and its impact on the phase stabilization of all-inorganic cesium lead iodide perovskites. Matter. 2023;6(7):2368-2382. https://doi.org/10.1016/j.matt.2023.05.027
24. Zhang J, Yin C, Yang F, Yao Y, Yuan F, Chen H, et al. Highly Luminescent and Stable CsPbI3 Perovskite Nanocrystals with Sodium Dodecyl Sulfate Ligand Passivation for Red-Light-Emitting Diodes. J Phys Chem Lett. 2021;12(9):2437-2443. https://doi.org/10.1021/acs.jpclett.1c00008
25. Chen LC, Chang YT, Tien CH, Yeh YC, Tseng ZL, Lee KL, et al. Red Light-Emitting Diodes with All-Inorganic CsPbI3/TOPO Composite Nanowires Color Conversion Films. Nanoscale Res Lett. 2020;15:157. https://doi.org/10.1186/s11671-020-03430-w
26. Chen D, Huang D, Yang M, Xu K, Hu J, Liang S, et al. Precursor chemistry towards highly efficient and phase-stable red emitting CsPbI3 perovskite nanocrystals. Nano Res. 2022;15(1):644-652. https://doi.org/10.1007/s12274-021-3538-1
27. Wen Z, Zhai W, Liu C, Lin J, Yu C, Huang Y, et al. Controllable synthesis of CsPbI3 nanorods with tunable photoluminescence emission. RSC Adv. 2019;9(43):24928-24934. https://doi.org/10.1039/C9RA04600C
28. Chung I, Song JH, Im J, Androulakis J, Malliakas CD, Li H, et al. CsSnI3: Semiconductor or metal? High electrical conductivity and strong near-infrared photoluminescence from a single material. J Am Chem Soc. 2012;134(20):8579-8587. https://doi.org/10.1021/ja301539s
29. Da Silva EL, Skelton JM, Parker SC, Walsh A. Phase stability and transformations in the halide perovskite CsSnI3. Phys Rev B. 2015;91(14):144107. https://doi.org/10.1103/PhysRevB.91.144107
30. Monacelli L, Marzari N. First-Principles Thermodynamics of CsSnI3. Chem Mater. 2023;35(4):1702-1709. https://doi.

org/10.1021/acs.chemmater.2c03475
31. Ali MS, Das S, Abed YF, Basith MA. Lead-free CsSnCl3 perovskite nanocrystals: Rapid synthesis, experimental characterization and DFT simulations. Phys Chem Chem Phys. 2021;23(39):22184-22198. https://doi.org/10.1039/D1CP02666F
32. Adib MA, Sharmin F, Basith MA. Tuning the morphology, stability and optical properties of CsSnBr3 nanocrystals through bismuth doping for visible-light-driven applications. Nanoscale Adv. 2023;5(22):6194-6209. https://doi.org/10.1039/D3NA00309D
33. Yasmeen F, Tarek M, Basith MA. Moisture-Stable CsSnBr2Cl Halide Perovskite: Electrochemical Insights in Aqueous Environments. ACS Appl Mater Interfaces. 2024;16(35):47535-47550. https://doi.org/10.1021/acsami.4c08313
34. Lin S, Zhang B, Lü TY, Zheng JC, Pan H, Chen H, et al. Inorganic Lead-Free B-γ-CsSnI3 Perovskite Solar Cells Using Diverse Electron-Transporting Materials: A Simulation Study. ACS Omega. 2021;6(41):26689-26698. https://doi.org/10.1021/acsomega.1c04096
35. Zhang M, Chen K, Wei Y, Hu W, Cai Z, Zhu J, et al. Strategies for Optimizing the Morphology of CsSnI3 Perovskite Solar Cells. Crystals (Basel). 2023;13(3):410. https://doi.org/10.3390/cryst13030410
36. Ye T, Wang K, Hou Y, Yang D, Smith N, Magill B, et al. Ambient-Air-Stable Lead-Free CsSnI3 Solar Cells with Greater than 7.5% Efficiency. J Am Chem Soc. 2021;143(11):4319-4328. https://doi.org/10.1021/jacs.0c13069
37. Yao H, Zhou F, Li Z, Ci Z, Ding L, Jin Z. Strategies for Improving the Stability of Tin-Based Perovskite (ASnX3) Solar Cells. Adv Sci. 2020;7(10):1903540. https://doi.org/10.1002/advs.201903540
38. Cao F, Tian W, Wang M, Wang M, Li L. Stability enhancement of lead-free CsSnI3 perovskite photodetector with reductive ascorbic acid additive. InfoMat. 2020;2(3):577-584. https://doi.org/10.1002/inf2.12074
39. Benaicha I, Amraoui S, Mhalla J, Ait-Alla Y, Diyagh H, Simassa M, et al. Enhanced structural stability and optoelectronic properties of lead-free α-phase CsSnI3 perovskite via Zn and Cu doping. Results Eng. 2025;27:106845. https://doi.org/10.1016/j.rineng.2025.106845
40. Dilshod N, Anushervon A, Amondulloi B, Iskandar R, Kholmurodov K. Preparation of Air Stable Lead-free CsSnI3 Perovskites: Synthesis Based on CsI and SnCl2 Solutions. J Mod Nanotechnol. 2024;4:7. https://doi.org/10.53964/jmn.2024007
41. Waleed A, Tavakoli MM, Gu L, Hussain S, Zhang D, Poddar S, et al. All inorganic cesium lead iodide perovskite nanowires with stabilized cubic phase at room temperature and nanowire array-based photodetectors. Nano Lett. 2017;17(8):4951-4957. https://doi.org/10.1021/acs.nanolett.7b02101
42. Shen Q, Ripolles TS, Even J, Ogomi Y, Nishinaka K, Izuishi T, et al. Slow hot carrier cooling in cesium lead iodide perovskites. Appl Phys Lett. 2017;111(15):153903. https://doi.org/10.1063/1.4991993
43. Liu F, Zhang Y, Ding C, Kobayashi S, Izuishi T, Nakazawa N, et al. Highly Luminescent Phase-Stable CsPbI3 Perovskite Quantum Dots Achieving Near 100% Absolute Photoluminescence Quantum Yield. ACS Nano. 2017;11(10):10373-10383. https://doi.org/10.1021/acsnano.7b05442
44. Farzaneh A, Abdi MR, Saraee KRE, Mostajabaldaavati M, Quaranta A. The preparation of cesium-iodide thin films via sol-gel method for the detection of ionizing radiation. J Solgel Sci Technol. 2016;78(2):313-321. https://doi.org/10.1007/s10971-016-3959-6
45. Burschka J, Pellet N, Moon SJ, Humphry-Baker R, Gao P, Nazeeruddin MK, et al. Sequential deposition as a route to high-performance perovskite-sensitized solar cells. Nature. 2013;499(7458):316-319. https://doi.org/10.1038/nature12340
46. Pradhan N. Growth of Lead Halide Perovskite Nanocrystals: Still in Mystery. ACS Phys Chem Au. 2022;2(4):268-276. https://doi.org/10.1021/acsphyschemau.2c00001
47. Dutta A, Dutta SK, Das Adhikari S, Pradhan N. Phase-Stable CsPbI3 Nanocrystals: The Reaction Temperature Matters. Angew Chem Int Ed Engl. 2018;57(29):9083-9087. https://doi.org/10.1002/anie.201803701
48. Stelmakh A, Aebli M, Baumketner A, Kovalenko MV. On the Mechanism of Alkylammonium Ligands Binding to the Surface of CsPbBr3 Nanocrystals. Chem Mater. 2021;33(15):5962-5973. https://doi.org/10.1021/acs.chemmater.1c01081
49. Zhou Y, Garces HF, Senturk BS, Ortiz AL, Padture NP. Room temperature "one-pot" solution synthesis of nanoscale CsSnI3 orthorhombic perovskite thin films and particles. Mater Lett. 2013;110:127-129. https://doi.org/10.1016/j.matlet.2013.08.011
50. Mahesh KPO, Chang CY, Hong WL, Wen TH, Lo PH, Chiu HZ, et al. Lead-free cesium tin halide nanocrystals for light-emitting diodes and color down conversion. RSC Adv. 2020;10(60):37161-37167. https://doi.org/10.1039/D0RA06139E
51. Jellicoe TC, Richter JM, Glass HFJ, Tabachnyk M, Brady R, Dutton SE, et al. Synthesis and Optical Properties of Lead-Free Cesium Tin Halide Perovskite Nanocrystals. J Am Chem Soc. 2016;138(9):2941-2944. https://doi.org/10.1021/jacs.5b13470
52. Chen LJ, Lee CR, Chuang YJ, Wu ZH, Chen C. Synthesis and Optical Properties of Lead-Free Cesium Tin Halide Perovskite Quantum Rods with High-Performance Solar Cell Application. J Phys Chem Lett. 2016;7(24):5028-5035. https://doi.org/10.1021/acs.jpclett.6b02344
53. Triloki, Garg P, Rai R, Singh BK. Structural characterization of as-deposited cesium iodide films studied by X-ray diffraction and transmission electron microscopy techniques. Nucl Instrum Methods Phys Res A. 2014;736:128-134. https://doi.org/10.1016/j.nima.2013.10.075
54. Sutton RJ, Filip MR, Haghighirad AA, Sakai N, Wenger B, Giustino F, et al. Cubic or Orthorhombic? Revealing the Crystal Structure of Metastable Black-Phase CsPbI3 by Theory and Experiment. ACS Energy Lett. 2018;3(8):1787-1794. https://doi.org/10.1021/acsenergylett.8b00672
55. Dimesso L, Das C, Stöhr M, Jaegermann W. Investigation of cesium tin/lead iodide (CsSn1−xPbxI3) systems. Mater Res Bull. 2017;85:80-89. https://doi.org/10.1016/j.materresbull.2016.08.052
56. Zhang L, Zhou H, Chen Y, Zheng Z, Huang L, Wang C, et al. Spontaneous crystallization of strongly confined CsSnxPb1-xI3 perovskite colloidal quantum dots at room temperature. Nat Commun. 2024;15:905. https://doi.org/10.1038/s41467-024-45945-1
57. Bindu P, Thomas S. Estimation of lattice strain in ZnO nanoparticles: X-ray peak profile analysis. J Theor Appl Phys. 2014;8(4):123-134. https://doi.org/10.1007/s40094-014-0141-9
58. Dawson M, Ribeiro C, Morelli MR. A Review of Three-Dimensional Tin Halide Perovskites as Solar Cell Materials. Mater Res. 2022;25:e20210441. https://doi.org/10.1590/1980-5373-mr-2021-0441
59. Perez De Berti IO, Cagnoli MV, Pecchi G, Alessandrini JL, Stewart SJ, Bengoa JF, et al. Alternative low-cost approach to the synthesis of magnetic iron oxide nanoparticles by thermal decomposition of organic precursors. Nanotechnology. 2013;24(17):175601. https://doi.org/10.1088/0957-4484/24/17/175601
60. Zhao Y, Yao Z, Snow CD, Xu Y, Wang Y, Xiu D, et al. Stable fluorescence of Eu3+ complex nanostructures beneath a protein skin for potential biometric recognition. Nanomaterials (Basel). 2021;11(9):2462. https://doi.org/10.3390/nano11092462

61. Ibarra J, Melendres J, Almada M, Burboa MG, Taboada P, Juárez J, et al. Synthesis and characterization of magnetite/PLGA/chitosan nanoparticles. Mater Res Express. 2015;2(9):095010. https://doi.org/10.1088/2053-1591/2/9/095010
62. Liascukiene I, Aissaoui N, Asadauskas SJ, Landoulsi J, Lambert JF. Ordered nanostructures on a hydroxylated aluminum surface through the self-assembly of fatty acids. Langmuir. 2012;28(11):5116-5124. https://doi.org/10.1021/la2051542
63. Li G, Rivarola FWR, Davis NJLK, Bai S, Jellicoe TC, De La Peña F, et al. Highly Efficient Perovskite Nanocrystal Light-Emitting Diodes Enabled by a Universal Crosslinking Method. Adv Mater. 2016;28(18):3528-3534. https://doi.org/10.1002/adma.201600064
64. Böer KW, Pohl UW. Excitons. In: Semiconductor Physics. Springer; 2023. https://doi.org/10.1007/978-3-031-18286-0
65. Zhai W, Lin J, Li Q, Zheng K, Huang Y, Yao Y, et al. Solvothermal Synthesis of Ultrathin Cesium Lead Halide Perovskite Nanoplatelets with Tunable Lateral Sizes and Their Reversible Transformation into Cs4PbBr6 Nanocrystals. Chem Mater. 2018;30(11):3714-3721. https://doi.org/10.1021/acs.chemmater.8b00612
66. Haryński Ł, Olejnik A, Grochowska K, Siuzdak K. A facile method for Tauc exponent and corresponding electronic transitions determination in semiconductors directly from UV-Vis spectroscopy data. Opt Mater (Amst). 2022;127:112205. https://doi.org/10.1016/j.optmat.2022.112205